

RESEARCH ARTICLE Characterizing the eddy field in the Arctic Ocean halocline

10.1002/2014JC010488

Key Points:

- More than 100 anticyclones in the Arctic halocline were sampled from 2004 to 2013
- Eddy diameters are consistent with the Rossby deformation radius
- Four classes of eddies have distinct properties and formation mechanisms

Correspondence to:

M. Zhao,
mengnan.zhao@yale.edu

Citation:

Zhao, M., M.-L. Timmermans, S. Cole, R. Krishfield, A. Proshutinsky, and J. Toole (2014), Characterizing the eddy field in the Arctic Ocean halocline, *J. Geophys. Res. Oceans*, 119, doi:10.1002/2014JC010488.

Received 3 OCT 2014

Accepted 21 NOV 2014

Accepted article online 27 NOV 2014

Mengnan Zhao¹, Mary-Louise Timmermans¹, Sylvia Cole², Richard Krishfield², Andrey Proshutinsky², and John Toole²

¹Department of Geology and Geophysics, Yale University, New Haven, Connecticut, USA, ²Woods Hole Oceanographic Institution, Woods Hole, Massachusetts, USA

Abstract Ice-Tethered Profilers (ITP), deployed in the Arctic Ocean between 2004 and 2013, have provided detailed temperature and salinity measurements of an assortment of halocline eddies. A total of 127 mesoscale eddies have been detected, 95% of which were anticyclones, the majority of which had anomalously cold cores. These cold-core anticyclonic eddies were observed in the Beaufort Gyre region (Canadian water eddies) and the vicinity of the Transpolar Drift Stream (Eurasian water eddies). An Arctic-wide calculation of the first baroclinic Rossby deformation radius R_d has been made using ITP data coupled with climatology; $R_d \sim 13$ km in the Canadian water and ~ 8 km in the Eurasian water. The observed eddies are found to have scales comparable to R_d . Halocline eddies are in cyclogeostrophic balance and can be described by a Rankine vortex with maximum azimuthal speeds between 0.05 and 0.4 m/s. The relationship between radius and thickness for the eddies is consistent with adjustment to the ambient stratification. Eddies may be divided into four groups, each characterized by distinct core depths and core temperature and salinity properties, suggesting multiple source regions and enabling speculation of varying formation mechanisms.

1. Introduction

Ocean eddies have significant influence on the lateral transport of heat, momentum, chemical tracers, nutrients, biological species, and anomalous water properties [see Carton, 2010]. In the Arctic Ocean, eddies have been observed at all depths and in all regions. Halocline eddies may be especially important in that they can reduce the stability of the highly stratified halocline, which isolates warmer deeper waters from the surface ocean in contact with sea ice. Eddies have been observed in large numbers throughout the halocline; a multitude of past studies are cited below. Manley and Hunkins [1985], for example, estimated that halocline eddies may cover $\sim 25\%$ of the Beaufort Sea (by area) and are a significant source of kinetic energy in the halocline.

In this paper, we analyze Ice-Tethered Profiler data to catalog and characterize halocline eddies across the Arctic Ocean. The Arctic halocline, spanning depths from around 50 to 250 m, between the base of the surface mixed layer and the Atlantic water layer (AWL), is characterized by a strong increase in salinity (and potential density) and varying temperature structures. The Canadian and Eurasian waters have distinct halocline structures (Figure 1), and their approximate division in the northern Canada Basin has been shown to vary over time [e.g., Steele and Boyd, 1998; Bjork et al., 2002]. The cold Eurasian water halocline derives from modification of the surface waters by inflowing Atlantic water (including by sea-ice melt when Atlantic water first enters the Arctic Ocean), as well as by river input, sea-ice growth/melt cycles, and air-sea exchange [Rudels et al., 1996]. The Canadian water halocline is incised by warm interleaving layers associated with water of Pacific Ocean origin. Further, some profiles exhibit a shallow temperature maximum immediately below the surface mixed layer, the near surface temperature maximum (NSTM), which is formed by solar absorption during summer, that is then trapped by the summer halocline formed when ice melts [e.g., Jackson et al., 2011]. Below the NSTM there can be a temperature minimum near the freezing temperature associated with the remnant winter mixed layer (rWML) formed from the previous winter's mixed layer. Below these layers in the Canadian water halocline lies the Pacific Summer Water layer (PSW), believed to be derived from Pacific inflows that are modified by surface buoyancy fluxes over the Chukchi Sea in summer [e.g., Steele et al., 2004; Timmermans et al., 2014]. The temperature minimum underlying the PSW characterizes the Pacific Winter Water layer (PWW)-Pacific origin water modified over the Chukchi Sea in winter [e.g., Coachman and Barnes, 1961; Jones and Anderson, 1986].

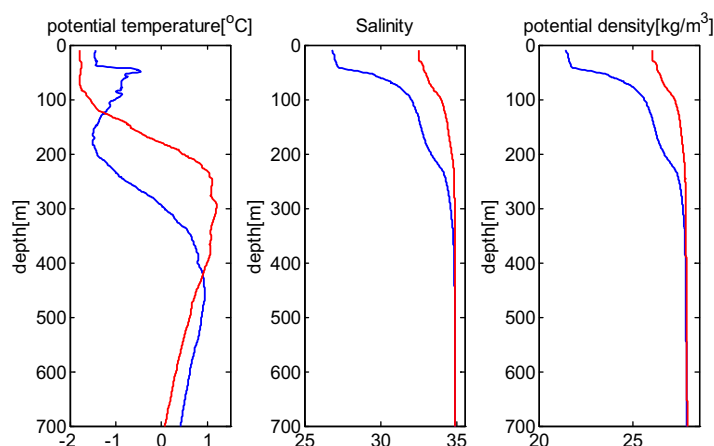


Figure 1. Representative potential temperature, salinity, and potential density in the upper Arctic Ocean, measured by ITPs. Red: Eurasian Water (ITP 14, 87.9° N, 17.0° W, October 2007); blue: Canadian Water (ITP 6, 76.7° N, 149.0° W, October 2007).

Halocline eddies are observed across all Arctic basins, with anticyclonic eddies overwhelmingly dominant [e.g., Aagaard et al., 1981; Manley and Hunkins, 1985; Timmermans et al., 2008]. Eddies can be both warm core and cold core, with the latter found in most cases [e.g., Manley and Hunkins, 1985]. Most past studies focus on eddies in the Canada Basin, where the eddies are concentrated in the halocline. These eddies are found to have core depths in the range of 30–300 m, azimuthal velocities in the range of 0.1–

0.3 m/s, diameters on the order of the Rossby deformation radius (10–20 km) and lifetimes from months to years [e.g., Hunkins, 1974; Manley and Hunkins, 1985; D’Asaro, 1988; Padman et al., 1990; Muench et al., 2000; Pickart et al., 2005; Plueddemann and Krishfield, 2007; Spall et al., 2008; Pickart and Stossmeister, 2008; Timmermans et al., 2008]. Eddies are believed to be generated by baroclinic instability of boundary currents, intense surface buoyancy fluxes, or frontal instabilities.

In one comprehensive study of halocline eddies, for example, Plueddemann and Krishfield [2007] analyzed velocity data from Ice-Ocean Environmental Buoys (IOEBs) operating in the Canadian Basin between 1992 and 1998 (a total of 44 months of buoy drift) and found 81 eddies, with 90% of them being anticyclones. These buoy velocity measurements were mostly from the periphery of the Beaufort Gyre, where eddies were found to be concentrated in the region of the Chukchi Plateau and southern Canada Basin. The majority of eddies were in the upper halocline centered around 140 m depth with azimuthal speeds of about 0.1–0.35 m/s, and diameters from 4 to 16 km. The faster eddies were typically taller and larger in diameter than the slower eddies. The shallowest and weakest eddies were observed over the Chukchi Plateau, with deeper and faster eddies sampled in the southern Canada Basin. Plueddemann and Krishfield [2007] suggest that the eddies they observed in the southern Canada Basin were predominantly generated by baroclinic instability of Beaufort Shelfbreak boundary currents.

In this paper, we analyze Ice-Tethered Profiler (ITP) measurements to develop an Arctic-wide assessment of halocline mesoscale eddies. To complement this study and assess the characteristic length scale for mesoscale flows (i.e., flows with horizontal scales on the order of the first baroclinic deformation radius, ~ 10 km in the Arctic Ocean), we use ITP data (coupled with climatology to extend ITP measurements to the full depth of the water column) to compute the first baroclinic Rossby deformation radius R_d . Measurements are introduced in section 2. In section 3, we calculate R_d across the Arctic Ocean. Section 4 outlines methods for detecting and characterizing the eddies. Eddy distributions, main characteristics, dynamical properties, and possible origins are presented in section 5. In section 6, we summarize and discuss our results in context with past studies.

2. Measurements

2.1. Ice-Tethered Profiler Measurements

ITPs consist of a surface buoy that sits on top of the sea ice, below which a wire-rope tether extends into the ocean. A profiling unit climbs up and down the tether measuring temperature, salinity, pressure, and in some cases velocity from a few meters below the base of the sea ice to about 750 m depth, returning 2–6 profiles per day. Measurements are transferred via satellite to servers at the Woods Hole Oceanographic Institution [see Krishfield et al., 2008, www.whoi.edu/itp; Toole et al., 2011]. A GPS unit in the surface buoy logs the location of the ITP every hour. Vertical data resolution is nominally 25 cm for a 1 Hz sampling rate and a profiling speed of about 25 cm/s. Given typical ice drift velocities of ~ 10 km/d, and ITP returns of

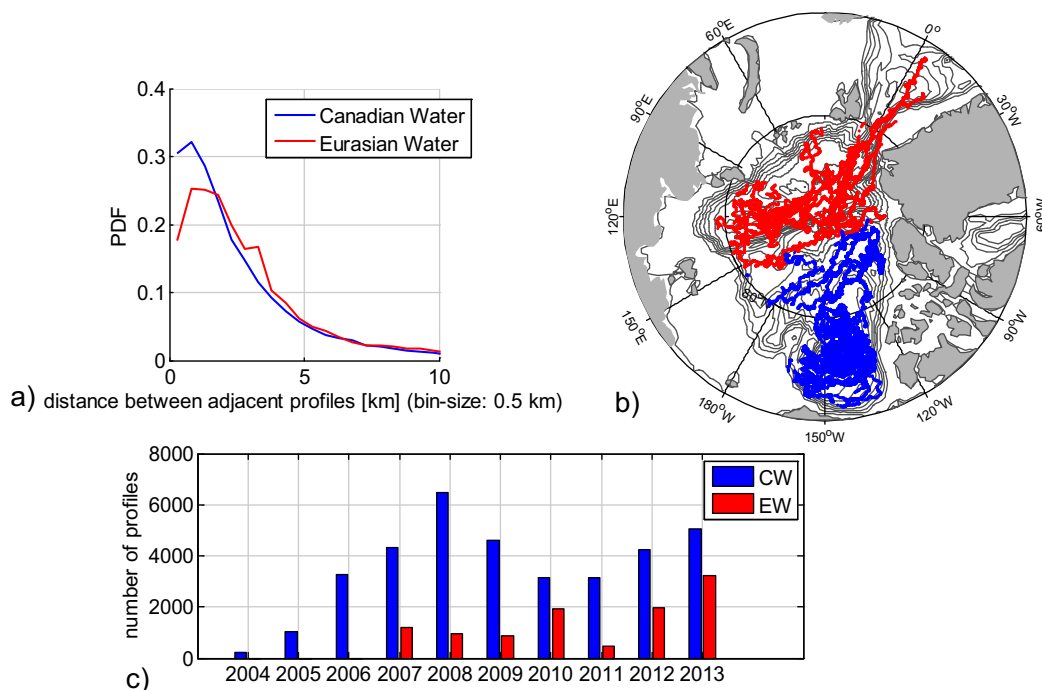


Figure 2. (a) PDF of ITP profile spacing [km]. Red: Eurasian Water (EW); blue: Canadian Water (CW). (b) Map showing location of ITP profiles from 2004 to 2013. (c) Number of ITP profiles in a given year.

two profiles or more per day, horizontal distances between adjacent vertical profiles are on the order of a few kilometers (Figure 2a).

The significant spatial coverage and horizontal CTD profile resolution, sufficient to detect scales at the small deformation radius of the Arctic Ocean, means ITP measurements enable an Arctic-wide assessment of the mesoscale eddy field. Due to year-round sea-ice cover over a significant fraction of the Arctic Ocean, satellite altimetry data (commonly used to examine the eddy field in the midlatitude ice-free oceans [e.g., Chaigneau *et al.*, 2011]) are not available, nor do satellite data allow study of the vertical structure of eddies. Eddy vertical structure may be studied using moored measurements, but spatial coverage is restricted. Further, typical hydrographic station spacings from ice breaker surveys have horizontal resolutions of several tens of kilometers between CTD profiles, not sufficient to resolve mesoscale eddies.

The first ITP was deployed in August 2004, and ITPs have been deployed every year since then, across the Arctic Ocean (Figure 2b). Each ITP is labeled with a distinct number, with low numbers indicating early deployments and the highest numbers referring to the more recent deployments. This paper investigates ITP data from the first measurement in 2004 through 31 December 2013; more than 46,000 profiles from 66 ITP systems are analyzed here (Figure 2c). For the first 5 years of the ITP data analyzed here, the fully processed data (i.e., including sensor response corrections, calibrations, and removal of erroneous profiles) are used. For the remaining years, ITP level 2 data are analyzed (see www.whoi.edu/itp/data); these are not the final processed data. We do not expect the level of processing to affect the results here as an examination of mesoscale eddies does not require detailed sensor lag corrections (i.e., temperature-salinity fine structure is not being analyzed) and spurious profiles are excluded.

2.2. Beaufort Gyre Exploration Project CTD Data and Climatology

Hydrographic survey data from the Beaufort Gyre Exploration Project (BGEP) are also used in this study. The calculation of the Rossby deformation radius requires CTD measurements extending the full water-column depth. BGEP CTD surveys (extending to the ocean bottom) were made over the Canada Basin every fall between 2003 and 2013 [see Proshutinsky *et al.*, 2009, www.whoi.edu/beaufortgyre/]. We compare the deep water column properties in BGEP CTD data to deep properties in the Environmental Working Group (EWG) Joint U.S.-Russian Atlas of the Arctic Ocean climatology for the decades 1950–1980 to show that it is

reasonable to use EWG climatology to extrapolate ITP profiles (with a maximum depth of around 750 m) to the bottom.

3. Calculation of the First Baroclinic Rossby Deformation Radius

The first baroclinic deformation radius is the dominant length scale for baroclinically unstable waves in a stratified flow and the natural horizontal scale of mesoscale instabilities, fronts, and eddies [e.g., Gill, 1982; Chelton *et al.*, 1998]. The Arctic-wide calculation of R_d not only provides an estimate of the horizontal scale of mesoscale eddies, it also dictates the model grid scale required to resolve mesoscale eddies in the Arctic Ocean.

A 1.5-layer model is often assumed for the calculation of R_d in the Arctic Ocean, with the two layers approximated to be separated by the halocline, $R_d \approx \frac{\sqrt{g'h}}{f}$, where $g' = \frac{\Delta\rho}{\rho_0}g$ is the reduced gravity for an upper layer of thickness h (above a lower layer much deeper than h), $\Delta\rho$ is the density difference between the two layers, ρ_0 is a reference density, and f is the Coriolis parameter. Approximating h to be 100 m for both the Canadian water and Eurasian water, $\Delta\rho$ to be 2.2 and 1.2 kg/m³, and ρ_0 to be 1025.5 and 1026.5 kg/m³ for the Canadian water and Eurasian water respectively, this yields $R_d \sim 13$ km for the Canadian water and ~ 8 km for the Eurasian water.

Chelton *et al.* [1998] solved the quasi-geostrophic equations for a given stratification to produce a nearly global map of R_d . Chelton *et al.* [1998] used the National Oceanographic Data Center (NODC) climatological average hydrographic product, but with a spatial range only extending to 65° N/S. Motivated by the absence of R_d estimates for the Arctic Ocean, Nurser and Bacon [2013] used the OCCAM global 1/12° model output [Marsh *et al.*, 2009] to calculate the deformation radius for the Arctic following the same method as Chelton *et al.* [1998]. Nurser and Bacon's [2013] analysis shows differences of up to 4 km between R_d computed from model output and R_d from limited CTD data in the central Arctic regions, with model output giving larger values due to model salinities being too fresh in the upper 300 m. Here, ITP measurements distributed over the central Arctic basins are combined with EWG climatology to produce an Arctic-wide map of R_d .

Our calculation of R_d follows the method of Chelton *et al.* [1998], and we refer the reader to that paper for details. In this calculation, the continuously stratified ocean (with $N^2(z) = -\frac{g}{\rho_0} \frac{\partial\rho}{\partial z}$) is taken to have a number m of discrete layers, corresponding to m normal modes. The baroclinic Rossby deformation radius of each mode is the wavelength of the corresponding internal gravity wave. $m = 0$ corresponds to the barotropic mode and $m = 1$ the first baroclinic mode and first baroclinic Rossby deformation radius R_d . We consider an f -plane and a rigid lid and flat bottom ocean of depth H .

Again, following Chelton *et al.* [1998], we also calculate R_d using the WKB approximation assuming stratification variations are small compared to the background stratification. In this case, the Rossby deformation radius for mode m is given by

$$R_{d_m}^{WKB} = \frac{1}{|f|m\pi} \int_{-H}^0 N(z') dz' \quad m \geq 1. \quad (1)$$

Although the WKB assumption is not appropriate in most cases due to the strong stratification at the base of the mixed layer, it is useful to show how R_d is influenced by the interplay between stratification, rotation, and the water column depth, important for understanding the geographical variation of R_d . The Arctic Ocean is effectively an f -plane and R_d is proportional to the vertical integral of $N(z)$. Because the deep basins are very weakly stratified, there is a near-linear relationship between R_d and water column depth in these regions. In shallow regions, stratification becomes more important in determining R_d . As we will show, variations in R_d between two regions of comparable depth can be attributed to differences in the strength of the halocline stratification between the two regions.

3.1. Extrapolating ITP Profiles to Full Depth

The calculation of R_d requires a density profile from the top to the bottom of the ocean; most ITP profiles extend between ~ 7 and 750 m depth. Given that mixed layer depths are mostly deeper than 15 m (e.g., Toole *et al.* [2010] who found mixed layer depth ~ 16 m in summer and ~ 24 m in winter in the Beaufort Gyre region), we use all ITP profiles with the shallowest measurement less than 15 m and take $N^2(z) = 0$

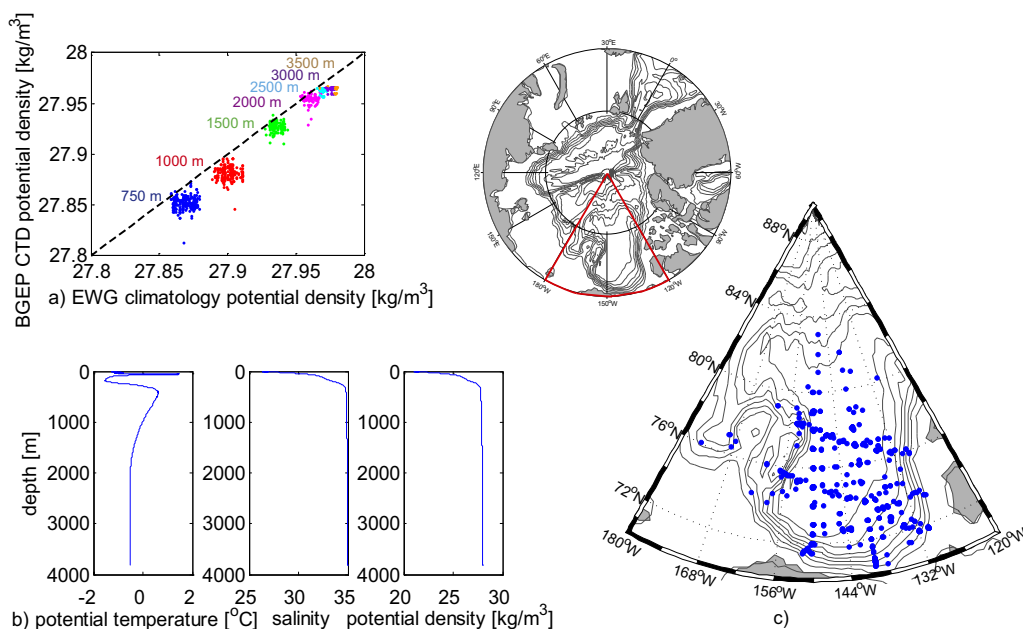


Figure 3. (a) Comparison of density from 750 m to the ocean bottom between all the BGEp CTD data (between 2003 and 2013) and the EWG climatology (between 1950 and 1980). The black line represents the one-to-one relationship. (b) Profiles of potential temperature, salinity, and potential density (referenced to the surface) from a CTD profile in the Central Canada Basin (9 August 2004) shown to illustrate the typical extremely weak stratification in the deep water. (c) Map of BGEp CTD profiles used in the comparison to EWG, where the area is marked by the red line on the inset map (see www.whoi.edu/beaufortgyre).

from the shallowest measurement to the surface. If the shallowest measurement is deeper than 15 m, the profile is not used in the calculations.

ITP density profiles must be extrapolated to the ocean bottom, and for this we assume that deep water properties are relatively unchanging on long time scales. Even on decadal time scales, we verify that the gradient in density below the core of the Atlantic Water Layer to the bottom can be considered time invariant for the purposes of our study (i.e., spatial patterns in this gradient observed in climatology can be used to extrapolate ITP profiles to the bottom). To illustrate this, we begin by comparing BGEp CTD data (those casts that extend to the bottom) to EWG climatology in the Beaufort Gyre region. For each BGEp CTD cast (from 2003 to 2013), we find the closest EWG grid point and compare density values through the deep water column (≥ 750 m). For each profile, there was some small (~ 0.02 kg/m³) density offset (between EWG and CTD), but no consistent spatial pattern to this offset. However, the density gradient between 750 m and the ocean bottom shows good agreement between BGEp CTD and EWG climatology (Figure 3a), and so it is reasonable to use the nearest EWG grid point profile to extrapolate each ITP profile to the bottom. For each deep EWG profile that is used to interpolate an ITP profile, we first apply an offset to the entire profile such that it matches the ITP density at 700 m. Note that EWG levels are at 700 and 750 m while many ITP profiles stop several meters shallower than 750 m. Therefore we chose 700 m as the matching level between EWG climatology and ITP profiles. In this way, a top to bottom $N(z)$ is computed from each extrapolated ITP density profile to solve for R_d using either the full calculation or WKB approximation.

3.2. Results

Across the Arctic Ocean, from the Canadian water to the Eurasian water, R_d decreases, following a similar pattern as found by Nurser and Bacon [2013] (Figures 4a and 4b). Nurser and Bacon [2013] attribute this pattern to the increase in the surface salinity (density) from the Canadian to Eurasian basins, resulting in a decreasing stratification trend. Within basins where the stratification varies little (e.g., the Canada Basin), the distribution of R_d largely follows the bathymetry, showing the influence of water column depth revealed in (1). R_d shows negligible seasonal variation, at least as indicated from one ITP (ITP 5) that drifted in the central Canada Basin over the deep abyssal plain with geographically close profiles over one year (not shown here). The seasonal variation of R_d is around 1 km: from a maximum of around 14.3 km in January to a minimum of around 13.4 km in September. There are not sufficient data to check the interannual variability of

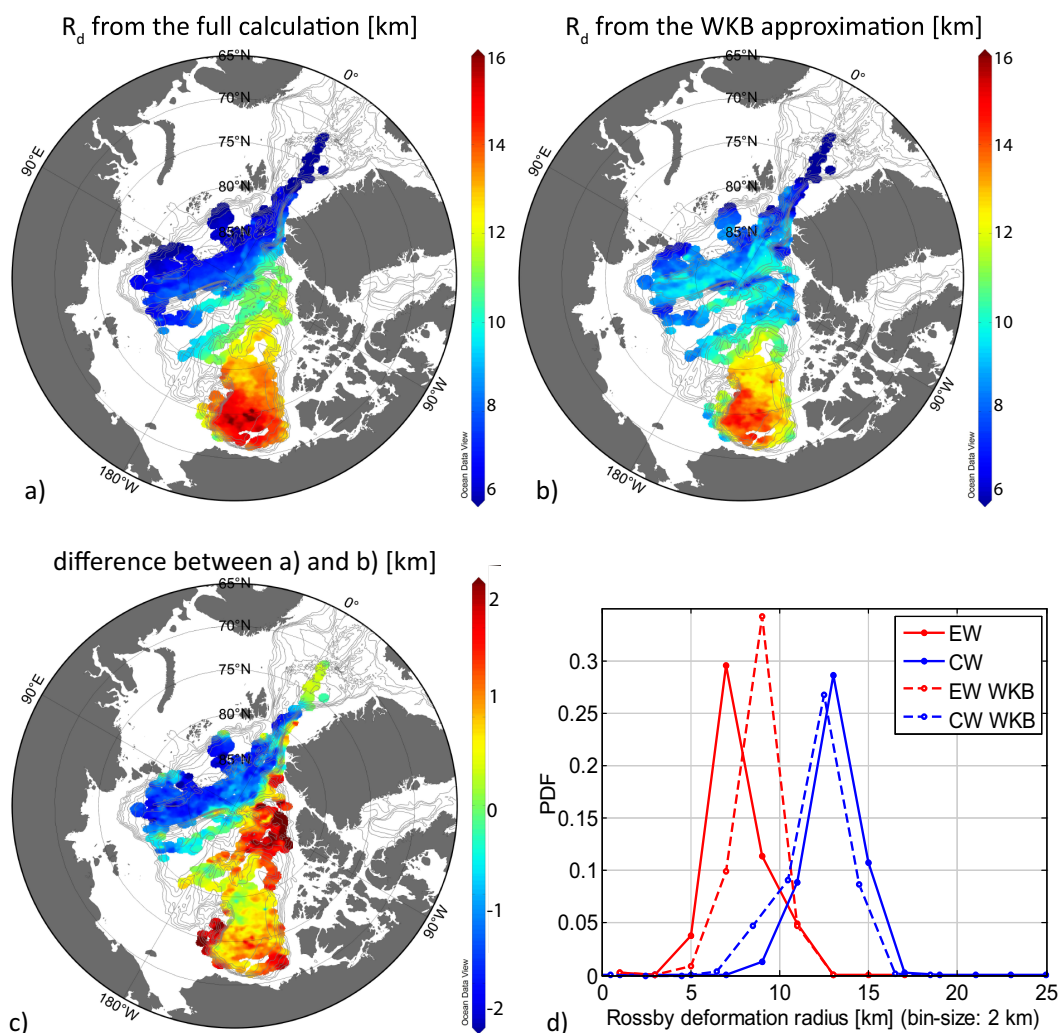


Figure 4. First baroclinic Rossby deformation radius R_d [km] calculated following the procedure outlined by *Chelton et al.* [1998] and using ITP profiles extrapolated to the bottom using EWG climatology. (a) R_d from the full calculation; (b) R_d calculated using the WKB approximation; (c) the difference between Figures 4a and 4b; (d) PDF of R_d , blue: Canadian water, red: Eurasian water; solid line: full calculation, dashed line: WKB approximation.

R_d across the Arctic Ocean. R_d of the Canadian water is about 13 km (12 km), and in the Eurasian water about 8 km (9 km) for the full eigenvalue problem (WKB approximation), similar to the result of the 1.5-layer approximation (Figure 4d). In the Canadian water, R_d from the full calculation is larger than that computed using the WKB method, while in the Eurasian water, the opposite holds (Figure 4c). In the Beaufort Gyre region, where *Nurser and Bacon's* [2013] model data appear to better represent their CTD data, our computed values of R_d are comparable to their values, while in the central Arctic Ocean, the region of highest discrepancy between their model data and their CTD measurements, our computed R_d are around 3 km smaller than *Nurser and Bacon's* [2013] values from model output, but similar to their calculations from CTD measurements.

4. Eddy Detection and Characterization

In this section we outline how mesoscale eddies are detected based on isopycnal displacement anomalies in the extensive ITP data set. ITP measurements allow for the detection of mesoscale eddies because the horizontal scale of mesoscale eddies (on the order of 10 km) is sufficiently greater than the horizontal resolution of the majority of ITP profiles (~ 2 km; Figure 2b). Typical ITP drift speeds (about 12 cm/s in the Eurasian Basin and 9 cm/s in the Canadian Basin) are faster than typical eddy advection speeds (assuming they

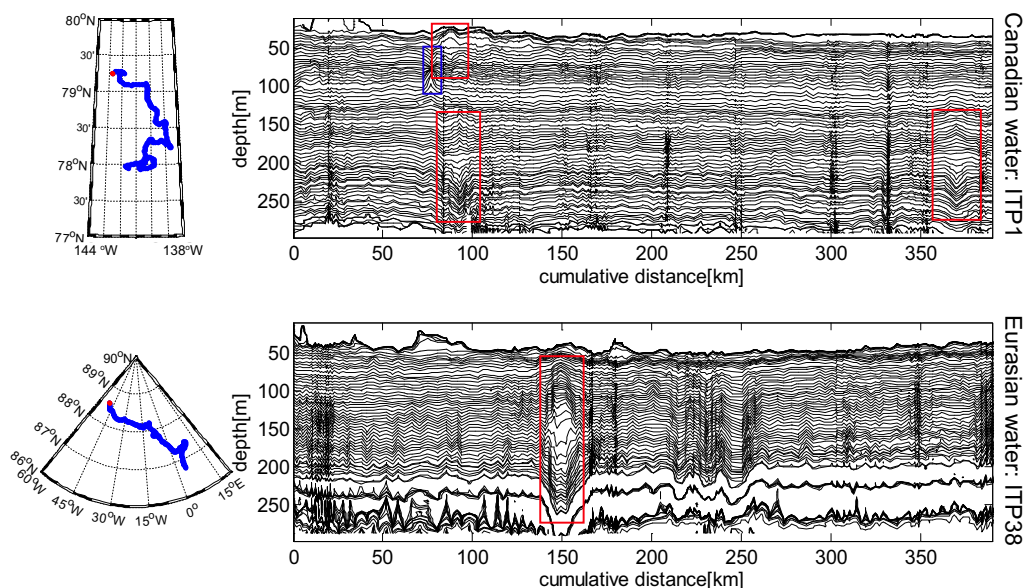


Figure 5. Example cumulative distance–density section from ITPs that drifted in Canadian Water (ITP 1) and Eurasian Water (ITP 38) in October to December 2005 and June to August 2010, respectively, along the tracks shown in the left panels (red dots mark the beginning of the drift and blue dots mark positions of subsequent profiles). Both ITPs returned four profiles per day with intervals of 6 h between profiles. Mean drift speeds were estimated to be about 7 km/d for ITP 1 and 8 km/d for ITP 38. Isopycnal values are chosen to be densities separated in depth by 4 m at the start profiles of the sections shown. Red boxes indicate anticyclonic eddies and the blue box shows a rare cyclonic eddy. The two shallower eddies highlighted in the top panel may be an example of dipole pair.

are advected passively in the Transpolar Drift Stream or Beaufort Gyre, flows with typical speeds of a few cm/s); in this respect, ITP measurements of mesoscale flows may be considered to be effectively synoptic. Further, the lifetimes of mesoscale eddies (on the order of several weeks to years) are much longer than the time taken for an ITP to transect an eddy (on the order of days).

Anticyclonic eddies are identified by convex-shaped isopycnal displacements in ITP density sections, and concave displacements for cyclonic eddies (Figure 5). Potential temperature is a useful additional indicator, with a clear, relatively uniform temperature anomaly (relative to the ambient water) in the center confirming the presence of an eddy. For eddy identification in the present study, both anomalous isopycnal displacements as well as anomalous core temperature are required to be present. An apparent eddy is only confirmed if the ITP drift track does not reverse direction during its transect—otherwise isopycnal displacements associated with an intrusion or a baroclinic front (for example) may appear to be an eddy (a “false” eddy). To conservatively identify a feature as an eddy, we require at least four profiles in a relatively straight drift track showing anomalous isopycnal displacements (and potential temperature). Here we are assuming that all features that meet the stated criteria are closed vortices, although we cannot rule out the possibility that the sampled feature is a meander.

From August 2004 to December 2013, 127 eddies were detected, 5 cyclonic, and 122 anticyclonic. Of these anticyclonic eddies, 7 had warm cores while 109 were cold-cored; the others exhibited combination core temperature structures (Figure 6). The remainder of this paper focuses on the cold-core anticyclonic eddies. In contrast to cold-core anticyclones, the limited number of warm-core anticyclones does not allow for a statistical analysis.

Once the cold-core eddies were identified, eddy core positions were estimated to be at the center of the convex-shaped isopycnal displacements (Figure 7a). Eddy core depths are defined to be the depth of the minimum temperature through the eddy core (Figure 7b), and eddy thicknesses are defined by the depth difference between the two buoyancy frequency maxima above and below the core (Figure 7c). Eddy diameters are defined as the distance between the bands of maximum azimuthal flow (see discussions to follow) on either side of the core (Figure 7d). The estimation of eddy core position and diameter may be biased when the ITP track does not transect the actual core of an eddy but rather skirts an edge. We estimate the error in both eddy core position and diameter as follows. Given our requirement for eddy detection of four

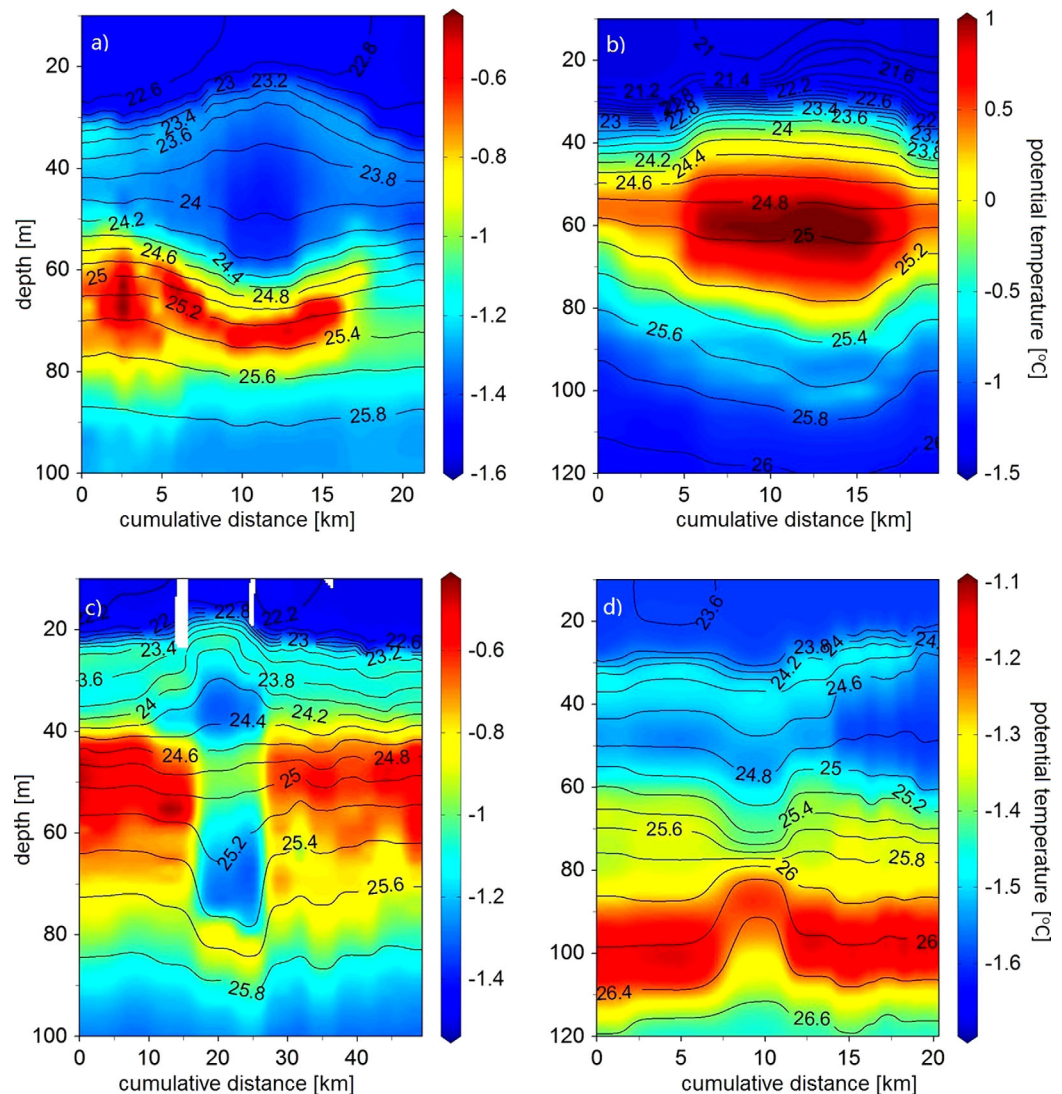


Figure 6. Representative potential temperature (color) and potential density (referenced to the surface) [kg/m^3 , contours] of all eddy types. (a) A cold-core eddy (ITP 3, 76.1°N , 136.0°W , December 2005); (b) a warm-core eddy (ITP 5, 76.1°N , 144.9°W , February 2007); (c) a combination-temperature-core eddy (ITP 64, 78.8°N , 141.0°W , October 2012); (d) a cyclonic eddy (ITP 1, 79.1°N , 140.6°W , November 2005).

profiles (in a straight drift track) measuring anomalous water properties, a typical length scale that will be measured is ~ 8 km (considering the typical profile spacing of ~ 2 km, Figure 2a). We anticipate that eddy horizontal length scales will be of the order of $R_d \sim 10$ km. In fact, examination of typical diameters (Figure 13b) shows this to be true. Comparing the lower bound (~ 8 km) to $R_d \sim 10$ km gives an error in the diameter of $\sim 20\%$, and a core position uncertainty of 3 km (although this leads to minimal discrepancies in reported core properties given the solid-body core structure). Of course, there are cases when an eddy is detected with horizontal length scale smaller than 8 km (i.e., when ITP drift was slow). In these cases, errors will be larger. We estimate, however, that 72% of the eddies sampled have diameter errors within 20% of R_d , and so inferred diameter errors less than 20%.

Eddy azimuthal velocities are calculated assuming the eddies are in cyclogeostrophic balance

$$-\frac{1}{\rho} \frac{\partial p}{\partial r} + \frac{v^2}{r} - fv = 0, \quad (2)$$

where the first term is the pressure gradient force per unit mass, the second term is the centrifugal acceleration, and the third term is the Coriolis acceleration. v is the azimuthal velocity, and r is the distance from the eddy core (taken to be at $r = 0$). Geostrophic velocity v_g between two ITP profiles is computed as

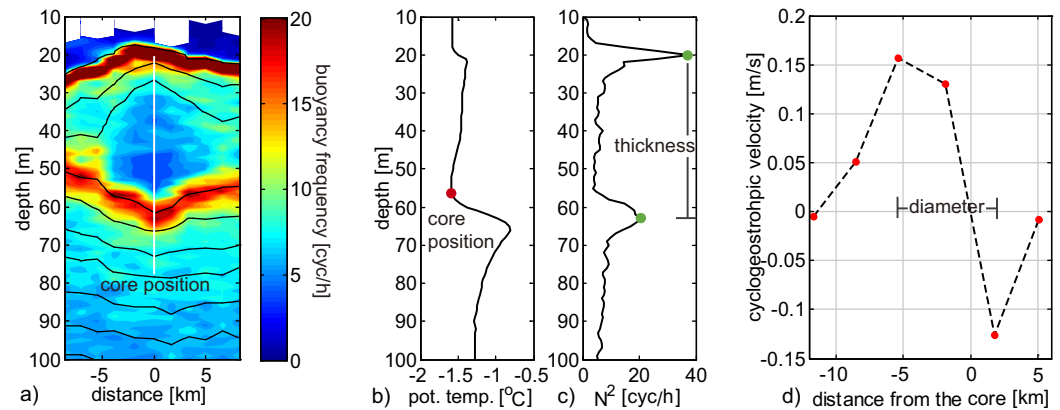


Figure 7. A typical cold-core anticyclone (ITP 2, 76.8° N, 137.3° W, September 2004) and definitions of eddy parameters.

$$fv_g = \frac{\Delta D}{\Delta x}, \quad (3)$$

where ΔD is the difference of dynamic height ($D = \int_{p_1}^{p_2} \frac{dp}{\rho}$, where p_1, p_2 are the pressures at the level of no motion and at the point of interest, respectively) between two adjacent upgoing ITP profiles, and Δx is the horizontal distance between the two profiles. Because the CTD sensors are located at the top of the ITP profiling unit, downgoing profiles can be influenced by its wake. Therefore, only data from ITP upgoing (odd profile numbers) are used in this calculation because small differences between up and downgoing profiles in the dynamic height field (calculated from temperature, salinity, and pressure) can result in spurious geostrophic velocities. For characterization of all other eddy properties, both up and downgoing profiles are used as other properties are not influenced by the small discrepancies between the two. For an anticyclone, the cyclogeostrophic velocity at a distance r from the eddy core can then be expressed as $v = \frac{\zeta}{2} (f - \sqrt{f^2 - \frac{4}{r} fv_g})$, with a theoretical maximum velocity of $\frac{\zeta}{2}$.

To compute dynamic heights, we assume a level of no motion of 300 m for most eddies, except for those profiles where deepest ITP measurements were shallower than 300 m, in which case the maximum depth is taken to be the level of no motion. Varying the choice of the level of no motion from 100 to 700 m (Figure 8d) suggests that its value is not a major influencing factor as long as this level is at least a few tens of meters deeper than the base of the eddy.

It is useful to compare ITP measured velocity (from the ITP-V) [see Cole *et al.*, 2014] with calculated cyclogeostrophic velocities as an ITP-V system transected a mesoscale eddy. Comparison between measured and calculated velocity (Figures 8a–8c) indicates that the cyclogeostrophic balance is an appropriate representation. In this case, the ITP-V measured velocity at 150 m depth was used in the integration (i.e., instead of assuming a level of no motion). These measured velocities were very small, about 0.03 m/s (the average value in profiles indicating the eddy, Figure 8e), much smaller than the eddy azimuthal velocities. Cyclogeostrophic velocities calculated through all eddy cores indicate that the observed anticyclones approximate a Rankine Vortex model (i.e., the eddy core is in solid body rotation with azimuthal velocity proportional to distance from the core, while outside the core the azimuthal velocity decays as $\frac{1}{r}$, e.g., Figure 8d).

Rossby numbers are computed to characterize the approximate dynamical balance of the eddies, with $R_o \sim 1$ indicating an eddy in cyclogeostrophic balance and $R_o \ll 1$ consistent with a quasi-geostrophic balance. Eddy Rossby numbers are calculated according to $R_o = \zeta/f$, where ζ is the maximum relative vorticity, and R is the eddy radius. In cylindrical coordinates, $\zeta = \frac{dv}{dr} + \frac{v}{r}$ can be scaled as $\frac{2U}{R}$ considering the eddy is in solid-body rotation [see, e.g., Manley and Hunkins, 1985; D'Asaro, 1988; Plueddemann and Krishfield, 2007; Timmermans *et al.*, 2008], where U is the maximum calculated azimuthal velocity through an eddy core. Therefore, the eddy Rossby number is appropriately defined as $R_o = \frac{2U}{fR}$.

5. Results

5.1. Eddy Distribution

Of the 109 cold-core anticyclonic eddies detected between 2004 and 2013, most were located in the Beaufort Gyre region and in the vicinity of the Transpolar Drift Stream, although there is likely some bias due to

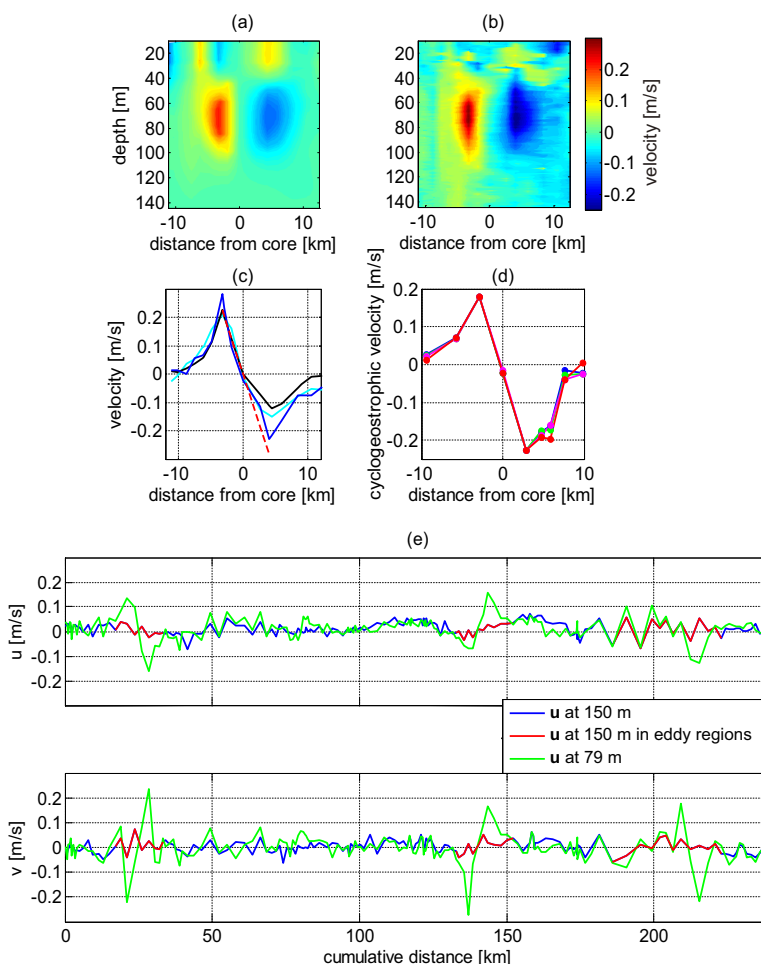


Figure 8. (a) Cyclogeostrophic velocity section for a typical eddy (sampled by ITP 35, 76.3° N, 136.9° W, November 2009) with a level of no motion of 150 m corresponding to the deepest measurements sampled by the ITP-V; (b) measured velocities for the same eddy (from the velocity sensor on ITP-V 35); (c) azimuthal velocities through the eddy core; black: calculated cyclogeostrophic velocity with a level of no motion of 150 m; cyan: calculated cyclogeostrophic velocity using the measured velocities (at 150 m); blue: measured velocities; red dashed: theoretical maximum cyclogeostrophic velocity; (d) calculated cyclogeostrophic velocity through a different eddy to that shown in Figures 8a–8c (sampled by ITP 3, 76.0° N, 136.0° W, December 2005) assuming different levels of no motion: blue, 700 m; green, 500 m; pink, 300 m; red, 100 m). (e) Measured velocities (from ITP-V 35) at the level of no motion (150 m, blue line, with red indicating eddy regions) and at a level corresponding to core depths of sampled eddies (79 m, green line) (positive u : eastward velocities; positive v : northward velocities).

the higher ITP profile density in these regions (Figure 9). Eddies are classified as Canadian water eddies or Eurasian water eddies depending upon the ambient water stratification in which they were found. Canadian water eddies may be divided into two groups: shallow (Figure 10a) and middepth (Figure 10b), as can Eurasian water eddies: shallow (Figure 10c) and middepth (Figure 10d). Different classes of eddies are characterized by different temperature and salinity properties, indicating they may have different source waters (Figure 11). Most shallow Canadian water eddies (eddy core depths < 80 m) were found in the northeast part of the Canada Basin, while middepth eddies (eddy core depths > 80 m) were mainly confined to the southwestern Canada Basin. We find that the distribution of eddies indicated no apparent relationship to season, although the data set is not yet large enough to make definitive conclusions.

Between 2005 and 2013, an ITP encountered around one eddy every ~ 1000 km (cumulative along-track distance, Figure 12), far fewer than the number detected by *Plueddemann and Krishfield* [2007] (they found around seven eddies every 1000 km). The IOEB drift analyzed by *Plueddemann and Krishfield* [2007] was mostly over the Chukchi Plateau and southern Canada Basin in the vicinity of boundary currents, which are eddy-generation regions. It may also be that direct measurements of velocity (analyzed by *Plueddemann and Krishfield* [2007]) are a better indicator of eddies than density measurements.

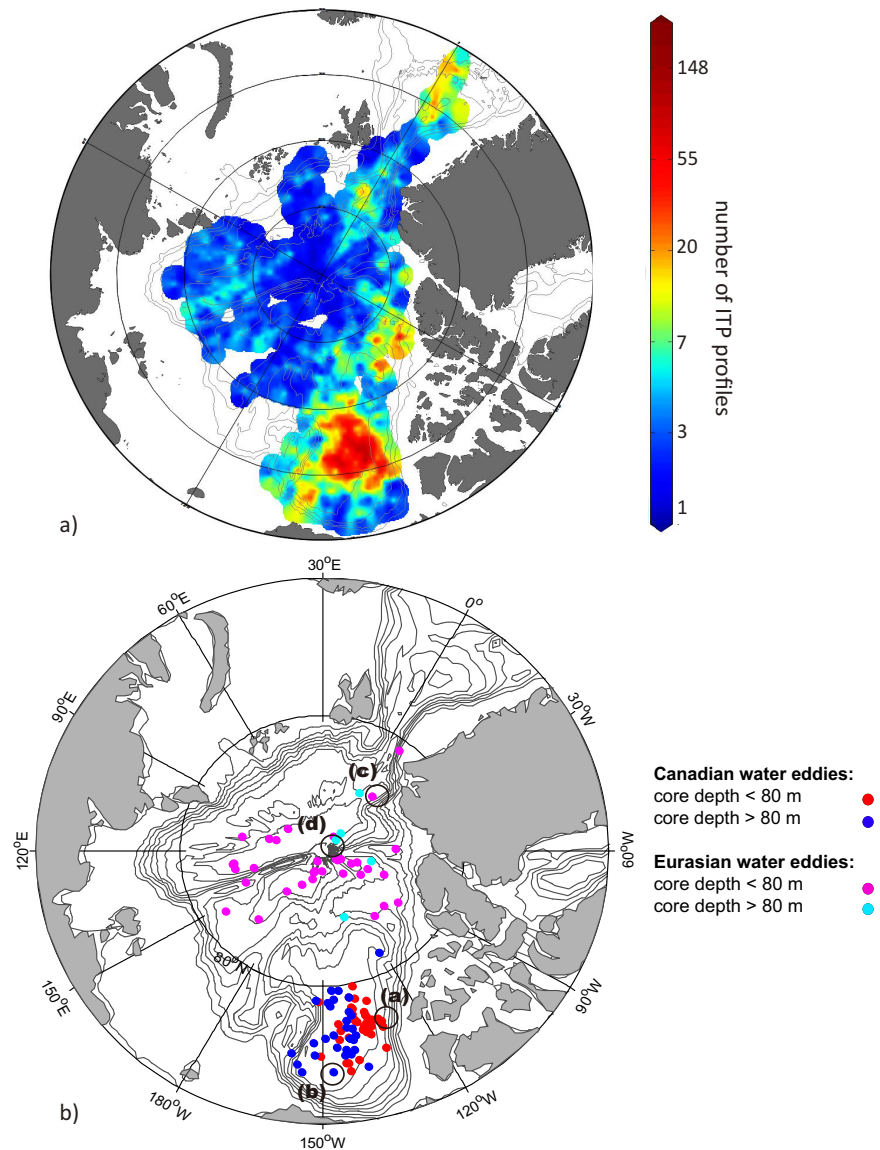


Figure 9. (a) The number of ITP profiles within a bin of 0.5° (note the color scale is logarithmic). (b) Core depth and distribution of a total of 109 cold-core anticyclonic eddies with numbered examples of typical eddies belonging to different eddy-types (shown in Figure 10). For Canadian water eddies, red: core depth above 80 m, blue: core depth below 80 m; for Eurasian water eddies, pink: core depth above 80 m; cyan-blue: core depth below 80 m.

5.2. Eddy Properties

Probability density functions (PDFs) of primary eddy parameters (core depth, diameter, azimuthal velocity, and Rossby number) document the general properties of the observed eddies (Figure 13). Canadian water eddy core depths have a bimodal distribution, centering around 50 m and 110 m (Figure 13a). The mode of 50 m is consistent with shallow eddies studied by *Timmermans et al.* [2008], while the 110 m mode is consistent with eddies studied by *Plueddemann and Krishfield* [2007] who, using direct velocity measurements, defined the eddy center depth to be the median depth of the maximum velocity in each profile. Eurasian water eddy core depths have a mode around 70 m, indicating that the majority of these eddies were located just beneath the Eurasian water mixed layer.

The diameter of observed eddies (Figure 13b) shows modes centered around 14 and 8 km for Canadian water eddies and 9 km for Eurasian water eddies. Eurasian water eddies and one mode of Canadian water eddies have horizontal scales comparable to R_d and consistent with larger deformation radii in the Canadian water compared to the Eurasian water. There is also a class of Canadian water eddies with smaller horizontal

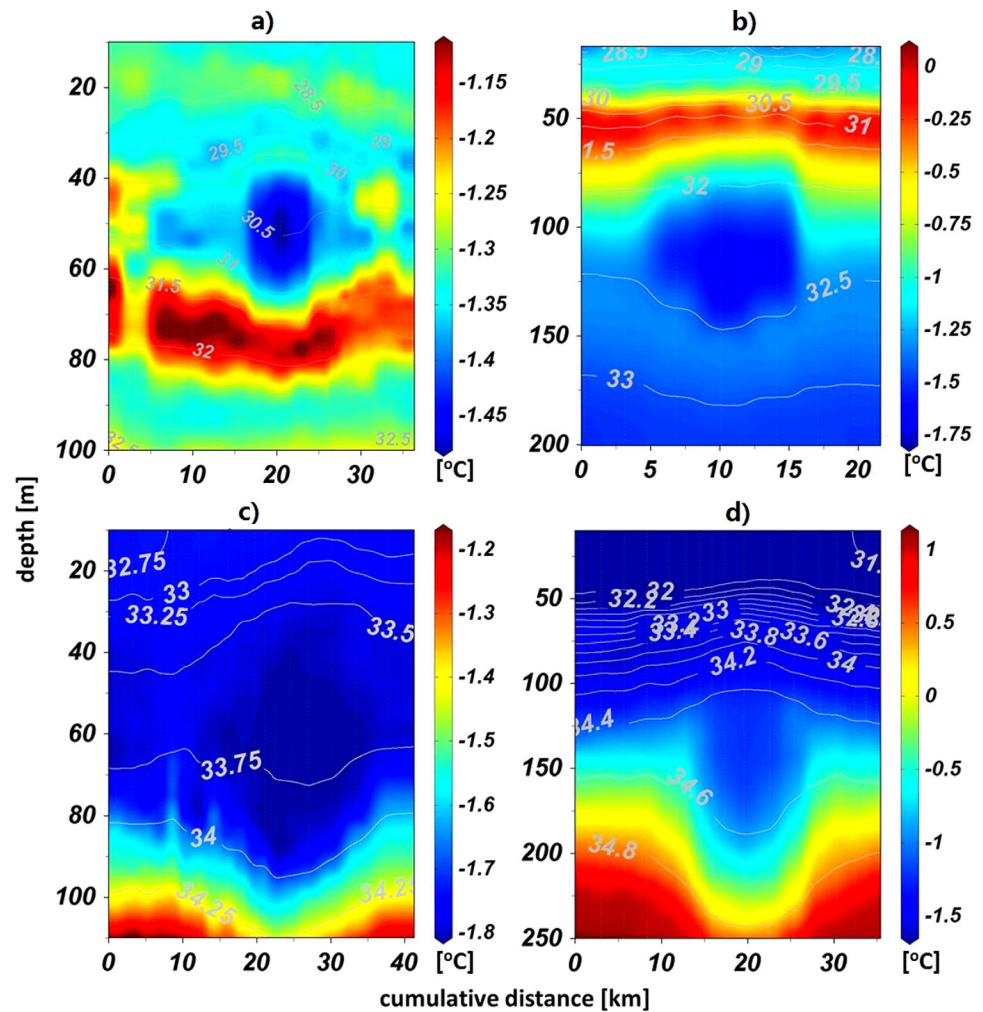


Figure 10. Potential temperature ($^{\circ}\text{C}$; colors) and salinity (white contours) sections for each of the five eddy-types (numbers at the top of each panel correspond to the numbers indicated in Figure 9). (a) A shallow Canadian water eddy (ITP 1; 29 July 2006; the eddy core resides above the warm Pacific summer water (the band of warm water in the potential temperature section between 60 and 80 m depth)). (b) A middepth Canadian water eddy (ITP 69; 5 September 2013; the eddy core resides in the Pacific water layer). (c) A shallow Eurasian water eddy (ITP 7; 25 August 2007; the eddy core resides above the warm Atlantic Water Layer (the band of warm water in the potential temperature section below 250 m depth)). (d) A middepth Eurasian water eddy (ITP 38; 11 July 2010; the eddy core resides near the warm Atlantic Water Layer).

scales, and varying core depths. The inferred smaller scales may result because the ITP transected the outer edge of those eddies. There is likely not a lower mode present for Eurasian water eddies because it may be even harder to detect a mesoscale eddy in the Eurasian water given the relatively smaller R_d in Eurasian water (horizontal profile resolution is about the same in each of the two basins). The diameter distribution for the Canadian water 110 m-core depth eddies (i.e., those middepth Canadian water eddies) shows a mode around 13 km (not shown), almost twice as large as eddies detected by *Plueddemann and Krishfield* [2007] (with the same definition for eddy diameters), who reported a mode around 7 km. Further, the range of diameters observed here (between 7 and 24 km) is approximately 5 km larger than the diameter range found by *Plueddemann and Krishfield* [2007].

Azimuthal velocities (Figure 13c) for Canadian water eddies have a trimmed mean value (eliminating the upper and lower 5%) of about 0.14 m/s, consistent with modes around 0.11 and 0.19 m/s. Eurasian water eddies have weaker azimuthal velocities, around 0.06 m/s. The azimuthal velocity distribution for the Canadian water 110 m-core depth eddies shows a mode of about 0.2 m/s (not shown), somewhat weaker than eddies found by *Plueddemann and Krishfield* [2007] (about 0.25 m/s); weaker velocities computed here might be caused by discrepancies between calculated cyclogeostrophic azimuthal velocities and directly

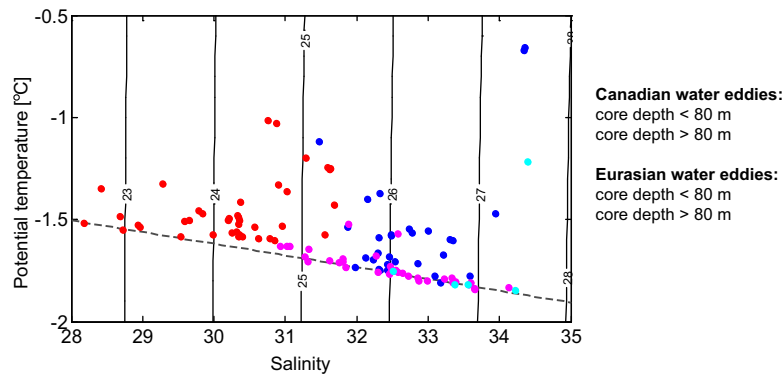


Figure 11. Potential temperature versus salinity of eddy core properties. Color coding indicates depths following Figure 9. The red line is the freezing line at zero pressure, and the near-vertical lines are isopycnals relative to zero pressure.

measured velocities. Combined with larger diameters of our eddies, it could also be that eddies measured by *Plueddemann and Krishfield* [2007] predominantly found in the Chukchi Plateau and Southern Canada Basin regions in the vicinity of the boundary currents, were closer to their origins, and there-

fore younger and more energetic than the eddies observed here (in the interior Canada Basin) which may have experienced some dissipation [e.g., *Muench et al.*, 2000; *Ou and Gordon*, 1986]. Eddy Rossby numbers (Figure 13d) for both Canadian and Eurasian water eddies have modes around 0.25 and 0.7, suggesting that most Eurasian water eddies and about half of Canadian water eddies are near geostrophic, while other eddies are in cyclogeostrophic balance. Overestimates of R_o occur when an ITP skirts the edge of an eddy. The distribution of R_o suggests a boundary between high and low R_o eddies around $R_o=0.5$, with the high R_o (i.e., cyclogeostrophic) eddies displaying a clear positive relationship between diameter and azimuthal velocity (Figure 14a), consistent with eddies studied by *Plueddemann and Krishfield* [2007] (this relationship is less well defined for low R_o eddies).

It is of note that the deeper eddies are thicker, consistent with a decrease in the stratification with depth in the Arctic halocline (Figure 14b) [see *Carpenter and Timmermans*, 2012]. *Carpenter and Timmermans* [2012] showed how eddies adjust their vertical structure to the ambient stratification and derived an expression for eddy scale height on an f -plane, assuming quasi-geostrophic potential vorticity conservation. They derived a relationship between eddy thickness δH , eddy diameter D , and the ambient stratification N (defined as the stratification adjacent to an eddy where the eddy azimuthal velocity decays to zero):

$$\delta H = 0.7 \frac{fD}{2N}, \tag{4}$$

as the height over which the velocity decays to 10% of the eddy velocity at its center depth. The distribution of eddy thickness measurements as a function of ambient stratification corresponds well with the theoretical prediction, showing that the vertical and horizontal scales of eddy adjustment are consistent with the ambient stratification (Figure 14c). When an eddy moves to a more weakly stratified environment, if its

diameter remains unchanged, the eddy grows taller in an efficient vertical transfer of momentum, with higher R_o eddies generally taller than predicted by the theory and vice versa for low R_o eddies.

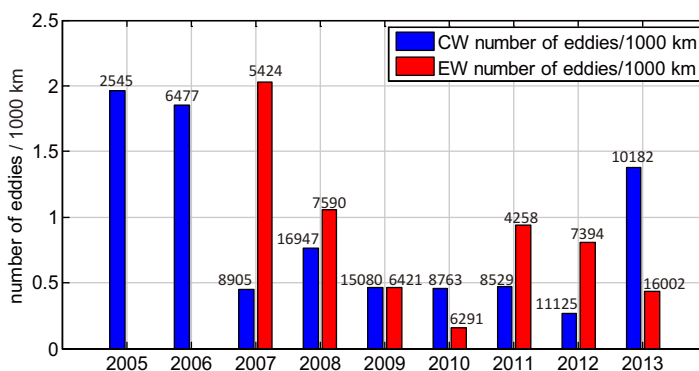


Figure 12. Number of eddy encounters per 1000 km along-track distance sampled by ITPs in the years shown. The number at the top of each bar indicates the corresponding total distance [km] sampled. 2004 is not shown because measurements are available only from August and September of that year.

5.3. Possible Eddy Origins
5.3.1. Canadian Water Eddies
 Shallow Canadian water eddies (e.g., Figure 10a) concentrate in the eastern Canada Basin and have properties most consistent with the shallow eddies studied by *Timmermans et al.* [2008],

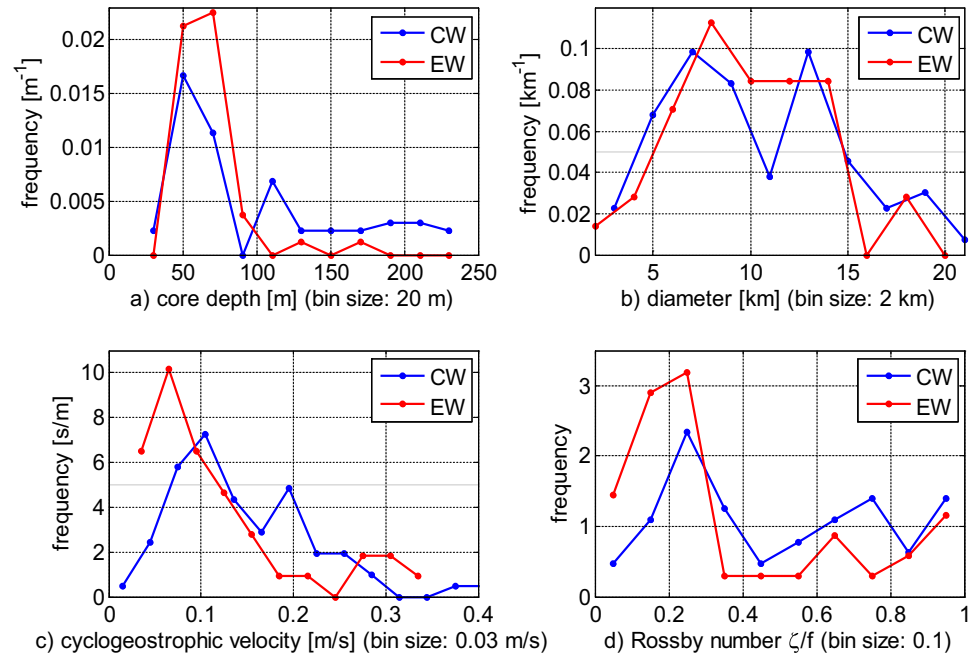


Figure 13. PDFs of primary eddy parameters. (a) Core depths (for a bin size of 20 m); (b) diameters (for a bin size of 2 km, four eddies had diameters >21 km, and these are not shown); (c) maximum cyclogeostrophic velocities (bin size 0.03 m/s, only one eddy had maximum cyclogeostrophic velocity >0.4 m/s and this is not shown); (d) Rossby numbers (bin size 0.1).

who suggested that these features are generated by ageostrophic baroclinic instability of a surface zonal front separating Canadian and Eurasian water. SCICEX data from 2000 show this front located around 78° N [Timmermans et al., 2008], with colder and saltier water on the northern side; the position of the front shows significant interannual variability [e.g., Timmermans et al., 2011]. ITP data show the front near 80° N in 2007, and near 83° N in 2009. Water masses on both sides of the front showed a freshening tendency, ~1.5 over these years; temperatures are around freezing. The freshening on the south side of the front is associated with an intensification of the anticyclonic Beaufort Gyre circulation and freshwater accumulation [see Proshutinsky et al., 2009]. The shallowest Canadian water eddies observed here show a similar core freshening from 2004 to 2008 with salinities decreasing from ~30.8 to ~28.5. These eddies are restricted to the eastern side of the basin. Nearly half of the Canadian water eddies are consistent with formation by baroclinic instability of this front, implicating the front as an important dynamical feature in the Arctic Ocean, transferring changes in surface-ocean properties to the halocline.

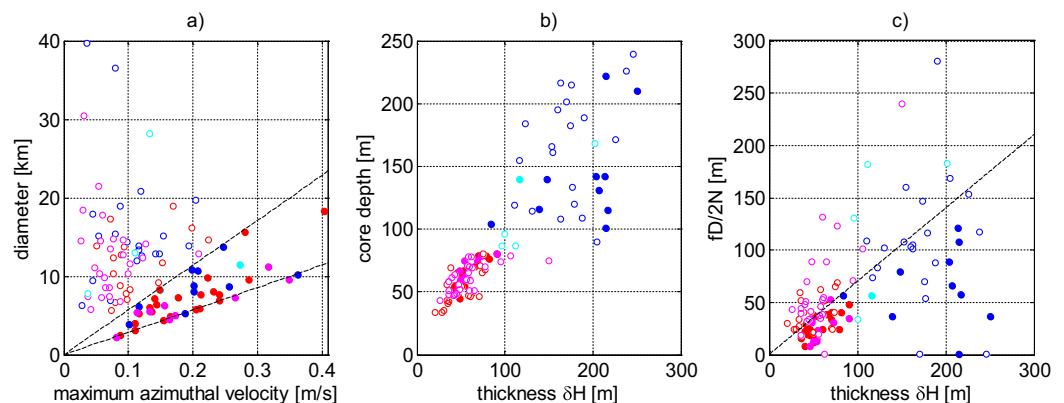


Figure 14. (a) Eddy maximum azimuthal velocities versus diameters. Top dashed line: $R_o = 0.5$; bottom dashed line: $R_o = 1$. (b) Eddy thicknesses versus core depths; (c) Eddy thicknesses versus $\frac{fd}{2N}$ (see equation (4)). Dashed line: theoretical relationship. Filled circles represent eddies with $R_o \geq 0.5$ and open circles with $R_o < 0.5$. Colors show different groups of eddies as in Figure 9.

After 2009, we did not observe any shallow eddies with core temperature near freezing. Further, the eddies observed in 2009–2013 were all at the deeper end of the range for shallow eddies, located near the central-southern part of the basin, and had saltier core properties ($S \sim 31$). Their presence is consistent with formation by baroclinic instability of the Chukchi-Beaufort shelfbreak jet or possibly with origins in coastal polynyas [e.g., *Pickart et al.*, 2005; *Pickart and Stossmeister*, 2008; *Chapman*, 1999].

Middepth Canadian water eddies (e.g., Figure 10b) are mainly distributed in the southwestern Canada Basin and have similar properties as the eddies modeled by *Spall et al.* [2008] and observed by *Pickart et al.* [2005], *Pickart and Stossmeister* [2008], and *Plueddemann and Krishfield* [2007], implying a similar formation mechanism—baroclinic instability of boundary currents in the Chukchi-Beaufort Sea. *Spall et al.* [2008] showed observations to be consistent with numerical experiments indicating that baroclinic instability of the spring configuration of the shelfbreak jet can be a source of these middepth Canadian water eddies. *Pickart et al.* [2005] sampled four anticyclonic cold-core eddies originating from the Beaufort/Chukchi shelfbreak jet of winter-transformed Bering Seawater from summer 2002 measurements. The eddies *Pickart et al.* [2005] observed had core potential temperatures around -1.7°C , and salinities around 33, somewhat colder and saltier than the eddies of comparable core depths sampled here. The source water properties imply that these eddies may be formed during the time period when winter-transformed Chukchi/Bering water is advected into the basin. This same middepth Canadian water eddy type was also observed between 1992 and 1998 by *Plueddemann and Krishfield* [2007], with the difference being that the eddies observed in our study generally have larger diameters and slower azimuthal velocities (note that *Plueddemann and Krishfield* [2007] did not have temperature and salinity information). Eddies detected here are further away from their inferred origins at the Chukchi/Beaufort shelfbreak jet. They have moved to the basin interior (although eddy advection or propagation mechanisms are unclear), having experienced some amount of spin-down and mixing with their ambient waters along their path, weakening their distinctive core properties and velocities.

Both warm and cold-core middepth anticyclonic eddies are observed in the Pacific Layer in the Canadian water (five warm-core anticyclones were observed in the Pacific Layer, e.g., Figure 6b). Cold-core eddies likely have origins in Pacific Winter Water boundary currents (e.g., boundary currents containing winter-transformed Bering/Chukchi water), while warm-core eddies are likely formed by instability of Pacific Summer Water boundary currents (e.g., boundary currents containing summer-modified Bering/Chukchi water) [*Pickart and Stossmeister*, 2008]. Not only do the core properties of these eddies allow for some inferences as to the variability in properties of their originating boundary currents, but they are also important in the connection between coastal regions and the basin interior, contributing to transporting biological and chemical material, such as nutrients, organic carbon, and zooplankton [e.g., *Mathis et al.*, 2007; *Watanabe*, 2011; *Nishino et al.*, 2011; *Watanabe et al.*, 2014]. It is of further interest that knowledge of the changing properties of boundary currents may allow us to put bounds on lifetimes of eddies generated by these currents.

5.3.2. Eurasian Water Eddies

Most past studies of Arctic eddies focus on Canadian water eddies; our ITP analysis indicates that the Eurasian halocline is also rich in eddies. Most Eurasian water eddies documented here (e.g., Figure 10c) were positioned immediately below the base of the mixed layer with weaker azimuthal velocities than Canadian water eddies. To our knowledge, previous observations of halocline Eurasian water eddies were limited to just a few examples. For example, *Polyakov et al.* [2012] present moored measurements of an “eddy-like structure” in the upper ~ 150 m over the Laptev Sea Slope in late December 2003 to early January 2004. *Woodgate et al.* [2000] found warm Atlantic Water eddies and cold middepth Eurasian water halocline eddies in moored measurements between 1995 and 1996 near the Lomonosov Ridge. *Woodgate et al.* [2000] attributed these eddies to baroclinic instability of fronts generated from coastal polynyas (as studied by *Chapman* [1999]). The generation of eddies by surface buoyancy forcing was also studied by *Bush and Woods* [2000] in both laboratory experiments and numerical/theoretical models. They outlined the generation of anticyclonic vortices at the base of the mixed layer as a response to convection in a lead. Numerical estimates by *Bush and Woods* [2000] using characteristic values of mass and momentum fluxes in a lead of width 100 m indicate that eddies formed in this way reside in the upper halocline (at the base of the mixed layer). Their characteristic diameters range from 4 to 20 km, in agreement with eddy scales reported here.

Middepth Eurasian water eddies are limited in numbers, and all of them locate in the vicinity of ridge features and in shelf regions. Their presence is consistent with formation either from instability of boundary

Table 1. Mean Properties of Different Cold-Core Anticyclone Eddy Types^a

Water Mass	Eastern CW	Southwestern CW	EW	EW
Possible origin	Surface front	Boundary currents	Surface buoyancy flux	Boundary currents
Number	30	40	34	5
R_o	0.54 ± 0.24	0.47 ± 0.27	0.35 ± 0.28	0.39 ± 0.23
Core depth (m)	53 ± 8.7	135 ± 47.2	63 ± 9.9	116 ± 32.7
Mean velocity (m/s)	0.14 ± 0.05	0.15 ± 0.06	0.10 ± 0.05	0.14 ± 0.08
Mean diameter (km)	9.5 ± 3.8	12.3 ± 4.1	10.5 ± 3.7	10.1 ± 2.2
Mean thickness (m)	48 ± 11.3	150 ± 53.4	56 ± 14.1	125 ± 39.1
Mean core T (°C)	-1.53 ± 0.04	-1.51 ± 0.22	-1.74 ± 0.06	-1.81 ± 0.03
Mean core salinity	29.9 ± 0.6	32.3 ± 0.7	32.5 ± 0.7	33.6 ± 0.7

^aTrimmed mean (eliminating the upper and lower 5%) and standard deviation are given.

currents or topographically steered flows in the vicinity of midbasin ridges. Note that even deeper eddies (i.e., below the halocline) have been studied in both the Eurasian water and the Canadian water [e.g., Carpenter and Timmermans, 2012; Aagaard et al., 2008].

6. Summary and Discussion

Mesoscale eddies are prevalent in the Arctic halocline and here are observed in the Beaufort Gyre region (Canadian water eddies) and in the vicinity of the Transpolar Drift Stream (Eurasian water eddies). Eddy properties are analyzed to obtain an Arctic-wide synthesis of the mesoscale eddy field over a decade of ITP measurements. Table 1 shows a summary of properties of the different types of eddies observed here.

We calculate R_d across the Arctic Ocean and show it is largest in the Canadian water (>13 km), with lower values characterizing the Eurasian water (~8 km) because the fresher (lower density) surface Canadian water results in a larger stratification. Changes in R_d in regions where the stratification varies little mainly follow the bathymetry (with deeper regions characterized by larger R_d). Our calculations of the deformation radii from ITP profiles (coupled with EWG climatology) across the Arctic fills in regions where R_d was not well estimated by model output and produces a reliable map of the deformation radius across the Arctic for further use in dynamical and modeling studies.

The eddies observed here have horizontal scales comparable to R_d , with Canadian water eddies larger than Eurasian water eddies, except for a group of smaller Canadian water eddies, which may be biased small because the ITPs did not transect the eddy cores. Eddies are in either near-geostrophic or cyclogeostrophic balance, with larger cyclogeostrophic eddies being stronger. The comparison between calculated azimuthal velocities and measured velocities (by an ITP-V) shows good agreement. Eddy velocities are well approximated by a Rankine Vortex. Vertical and horizontal scales of eddy adjustment are shown to be consistent with the ambient stratification.

We find eddies can be grouped into four types (two types of Canadian water eddies and two types of Eurasian water eddies) mainly distinguished by their core depths. Canadian and Eurasian water eddies have either shallow (<80 m) or middepth (>80 m) core depths. Different classes of eddies show different characterizing core temperature and salinity properties, suggesting different source waters.

The range of eddy core depths, locations, and core temperature-salinity properties found here are consistent with eddies observed in past studies, and origins and formation mechanisms for some eddies can be inferred from these. In the Canadian water, the shallowest eddies, likely generated by instability of a surface front, appear to be concentrated on the eastern side of the basin, and have near freezing core temperatures. Eddies likely generated by the instability of boundary currents in the Canada Basin concentrate on the southwestern side, with saltier core water and a range of core temperatures. Eurasian water eddies locate predominantly in the vicinity of ridge features and in shelf regions. Their presence is consistent with formation from instability of boundary currents or possibly with origins in coastal polynyas (more likely for shallower eddies).

Important topics for future study relate to understanding eddy formation, advection, spin-down processes, and lifetimes. Ocean eddy lifetimes are typically estimated from either biological and chemical tracers, or using the distance from the inferred origin region and assuming that the eddy translates with some known

mean flow [e.g., Manley and Hunkins, 1985; Kadko et al., 2008; Timmermans et al., 2008]. Eddy lifetime can also be estimated with some knowledge of the spin-down process. Eddy spin-down due to surface friction (in the sea ice-ocean boundary layer) has been studied theoretically by Ou and Gordon [1986] and Chao and Shaw [1996]. Ice-ocean friction causes an Ekman divergence above an anticyclonic eddy (in the Ekman layer adjacent to the sea ice). This leads to upwelling inside the eddy, and a lateral convergence toward the eddy bottom, generating cyclonic velocities which ultimately spin down the eddy. Ou and Gordon [1986] relate this spin-down time to the flattening of isopycnals, and obtain an expression for eddy spin-down time as a function of stratification, upwelling rate, eddy core depth and ice-ocean relative motion. In their theory, eddy velocities decrease with increasing diameters as the spin-down process proceeds. Using their expression (applicable for small R_o), we estimate lifetimes of the small R_o eddies observed here (that reside near the base of the mixed layer) to be in the range of 0.9 years to about 5 years.

Eddy spin-down can also take place in the absence of any sea ice influence but due to the vertical and horizontal velocity shear associated with the eddy and ambient flow, although this can be a small effect. Nonnegligible radial velocities may also play a role, and these can lead to horizontal flow convergence/divergence which generate vertical compensating flows and lead to exchange of eddy core waters with surrounding waters. For example, for one eddy detected by the ITP-V, radial velocities of the order of a few cm/s were observed inside the eddy. If we assume that the associated net horizontal divergence and the eddy horizontal scale remains unchanged, we estimate that it would have taken about 7 months for the eddy to exchange its waters completely with its surroundings. In addition, combined with the presumed generation site of the eddy (near the shelfbreak jet, around 157°W, 72°N) and assuming a mean background flow of around 0.02 m/s translating the eddy, the eddy was generated at least 14 months before being sampled by the ITP-V. Therefore, this eddy may have a lifetime of at least 21 months, in agreement with previous estimates of eddy lifetimes.

Further study of the rarer warm-core anticyclonic eddies and cyclones is also of interest. Theoretical studies suggest that eddies can sometimes form in a dipole, i.e., a cyclone-anticyclone pair [e.g., Manucharyan and Timmermans, 2013]. Understanding seasonal and interannual variability of the eddy field is important for estimating seasonal influences (such as sea ice) on eddy production, and varying heat and salt fluxes related to eddies, which can have an impact on the entire Arctic climate system.

Acknowledgments

Funding was provided by the National Science Foundation Polar Programs award ARC-1107623. The Ice-Tethered Profiler data were collected and made available by the Ice-Tethered Profiler Program [Toole et al., 2011; Krishfield et al., 2008] based at the Woods Hole Oceanographic Institution (<http://www.whoi.edu/itp>).

References

- Aagaard, K., L. K. Coachman, and E. Carmack (1981), On the halocline of the Arctic Ocean, *Deep Sea Res., Part A*, 28, 529–545.
- Aagaard, K., R. Andersen, J. Swift, and J. Johnson (2008), A large eddy in the central Arctic Ocean, *J. Geophys. Res.*, 35, L09601, doi:10.1029/2008GL033461.
- Bjork, G., J. Soderkvist, P. Winsor, A. Nikolopoulos, and M. Steele (2002), Return of the cold halocline layer to the Amundsen Basin of the Arctic Ocean: Implications for the sea ice mass balance, *Geophys. Res. Lett.*, 29(11), 1513–1516, doi:10.1029/2001GL014157.
- Bush, J. W. M., and A. W. Woods (2000), An investigation of the link between lead-induced thermohaline convection and arctic eddies, *Geophys. Res. Lett.*, 27, 1179–1182.
- Carpenter, J. R., and M.-L. Timmermans (2012), Deep mesoscale eddies in the Canada Basin, Arctic Ocean, *Geophys. Res. Lett.*, 39, L20602, doi:10.1029/2012GL053025.
- Carton, X. (2010), Oceanic vortices, *Lect. Notes Phys.*, 805, 61–108.
- Chaigneau, A., M. Le Texier, G. Eldin, C. Grados, and O. Pizarro (2011), Vertical structure of mesoscale eddies in the eastern South Pacific Ocean: A composite analysis from altimetry and Argo profiling floats, *J. Geophys. Res.*, 116, C11025, doi:10.1029/2011JC007134.
- Chao, S.-Y., and P.-T. Shaw (1996), Initialization, asymmetry, and spindown of Arctic eddies, *J. Phys. Oceanogr.*, 26, 2076–2092.
- Chapman, D. C. (1999), Dense water formation beneath a time-dependent coastal polynya, *J. Phys. Oceanogr.*, 29, 807–820.
- Chelton, D. B., R. A. DeSzoeke, M. G. Schlax, K. El. Niggar, and N. Siwertz (1998), Geographical variability of the first baroclinic Rossby radius of deformation, *J. Phys. Oceanogr.*, 28, 433–460.
- Coachman, L. K., and C. A. Barnes (1961), The contribution of Bering Sea Water to the Arctic Ocean, *Arctic*, 14, 147–161.
- Cole, S. T., M.-L. Timmermans, J. M. Toole, R. A. Krishfield, and F. T. Thwaites (2014), Ekman veering, internal waves, and turbulence observed under Arctic sea-ice, *J. Phys. Oceanogr.*, 44, 1306–1328.
- D'Asaro, E. A. (1988), Observations of small eddies in the Beaufort Sea, *J. Geophys. Res.*, 93, 6669–6684.
- Gill, A. E. (1982), *Atmosphere-Ocean Dynamics*, 662 p., Academic, San Diego, Calif.
- Hunkins, H. L. (1974), Subsurface eddies in the Arctic Ocean, *Deep Sea Res. Oceanogr. Abstr.*, 21, 1017–1033.
- Jackson, J. M., S. E. Allen, F. A. McLaughlin, R. A. Woodgate, and E. C. Carmack (2011), Changes to the near-surface waters in the Canada Basin, Arctic Ocean from 1993–2009, *J. Geophys. Res.*, 115, C10008, doi:10.1029/2011JC007069.
- Jones, E. P., and L. G. Anderson (1986), On the origin of the chemical properties of the Arctic Ocean halocline, *J. Geophys. Res.*, 91, 10,759–10,767.
- Kadko, D., R. S. Pickart, and J. Mathis (2008), Age characteristics of a shelf-break eddy in the western Arctic and implications for shelf-basin exchange, *J. Geophys. Res.*, 113, C02013, doi:10.1029/2007JC004429.

- Krishfield, R., J. Toole, A. Proshutinsky, and M.-L. Timmermans (2008), Automated Ice-tethered profilers for seawater observations under pack ice in all seasons, *J. Atmos. Oceanic Technol.*, *25*(11), 1092–2105.
- Manley, T. O., and H. L. Hunkins (1985), Mesoscale eddies in the Arctic Ocean, *J. Geophys. Res.*, *90*, 4911–4930.
- Manucharyan, G. E., and M.-L. Timmermans (2013), Generation and separation of mesoscale eddies from surface ocean fronts, *J. Phys. Oceanogr.*, *43*, 2545–2562.
- Marsh, R., B. A. de Cuevas, A. C. Coward, J. Jacquin, J.-M. Hirschi, Y. Aksenov, A. J. G. Nurser, and S. A. Josey (2009), Recent changes in the North Atlantic circulation simulated with eddy-permitting and eddy-resolving ocean models, *Ocean Modell.*, *28*, 226–239.
- Mathis, R. T., R. S. Pickart, D. A. Hansell, D. Kadko, and N. R. Bates (2007), Eddy transport of organic carbon and nutrients from the Chukchi shelf into the deep Arctic basin, *J. Geophys. Res.*, *112*, C05011, doi:10.1029/2006JC003899.
- Muench, R. D., J. T. Gunn, T. E. Whitledge, P. Schlosser, and W. Smethie Jr. (2000), An Arctic Ocean cold core eddy, *J. Geophys. Res.*, *105*, 23,997–24,006.
- Nishino, S., M. Itoh, Y. Kawaguchi, T. Kikuchi, and M. Aoyama (2011), Impact of an unusually large warm-core eddy on distributions of nutrients and phytoplankton in the southwestern Canada Basin during late summer/early fall 2010, *Geophys. Res. Lett.*, *38*, L16602, doi:10.1029/2011GL047885.
- Nurser, A. J. G., and S. Bacon (2013), Eddies length scales and the Rossby radius in the Arctic Ocean, *Ocean Sci. Discuss.*, *10*(5), 1807–1831, doi:10.5194/osd-10-1807-2013.
- Ou, H.-W., and A. L. Gordon (1986), Spin-down of baroclinic eddies under sea ice, *J. Geophys. Res.*, *91*, 7623–7630.
- Padman, L., M. Levine, T. Dillon, J. Morison, and R. Pinkel (1990), Hydrography and microstructure of an Arctic cyclonic eddy, *J. Geophys. Res.*, *21*, 707–719.
- Pickart, R. S., and G. Stossmeister (2008), Outflow of Pacific water from the Chukchi Sea to the Arctic Ocean, *Chin. J. Polar Oceanogr.*, *10*, 135–148.
- Pickart, R. S., T. J. Weingartner, L. J. Pratt, S. Zimmermann, and D. J. Torres (2005), Flow of winter transformed Pacific water into the Western Arctic, *Deep Sea Res., Part II*, *52*, 3175–3198.
- Plueddemann, A. J., and R. A. Krishfield (2007), Physical properties of eddies in the western Arctic (Unpublished manuscript), Woods Hole Oceanographic Institution, Woods Hole, Mass.
- Polyakov, I. V., A. V. Pnyushkov, R. Rember, V. V. Ivanov, Y.-D. Lenn, L. Padman, and E. C. Carmack (2012), Mooring-based observations of double-diffusive staircases over the Laptev Sea Slope, *J. Phys. Oceanogr.*, *42*, 95–109.
- Proshutinsky, A., R. Krishfield, M.-L. Timmermans, J. Toole, E. Carmack, F. McLaughlin, W. J. Williams, S. Zimmermann, M. Itoh, and K. Shimada (2009), Beaufort Gyre freshwater reservoir: State and variability from observation, *J. Geophys. Res.*, *114*, C00A10, doi:10.1029/2008JC005104.
- Rudels, B., L. G. Anderson, and E. P. Jones (1996), Formation and evolution of the surface mixed layer and the halocline of the Arctic Ocean, *J. Geophys. Res.*, *101*, 8807–8882.
- Spall, M. A., R. S. Pickart, P. S. Fratantoni, and A. J. Plueddemann (2008), Western Arctic shelfbreak eddies: Formation and transport, *J. Phys. Oceanogr.*, *38*, 1644–1668.
- Steele, M., and T. Boyd (1998), Retreat of the cold halocline layer in the Arctic Ocean, *J. Geophys. Res.*, *103*, 10,419–10,435.
- Steele, M., J. Morison, W. Ermold, I. Rigor, M. Ortmeyer, and K. Shimada (2004), Circulation of summer Pacific halocline water in the Arctic Ocean, *J. Geophys. Res.*, *109*, C02027, doi:10.1029/2003JC002009.
- Timmermans, M.-L., J. Toole, A. Proshutinsky, R. Krishfield, and A. Plueddemann (2008), Eddies in the Canada Basin, Arctic Ocean, observed from ice-tethered profilers, *J. Phys. Oceanogr.*, *38*, 133–145.
- Timmermans, M.-L., A. Proshutinsky, R. A. Krishfield, D. K. Perovich, J. A. Richter-Menge, T. P. Stanton, and J. M. Toole (2011), Surface freshening in the Arctic Ocean's Eurasian Basin: An apparent consequence of recent change in the wind-driven circulation, *J. Geophys. Res.*, *116*, C00D03, doi:10.1029/2011JC006975.
- Timmermans, M.-L., et al. (2014), Mechanisms of Pacific Summer Water variability in the Arctic's Central Canada Basin, *J. Geophys. Res. Oceans*, *119*, doi:10.1002/2014JC010273, in press.
- Toole, J. M., M.-L. Timmermans, D. K. Perovich, R. A. Krishfield, A. Proshutinsky, and J. A. Richter-Menge (2010), Influences of the ocean surface mixed layer and thermohaline stratification on Arctic Sea ice in the central Canada Basin, *J. Geophys. Res.*, *115*, C10018, doi:10.1029/2009JC005660.
- Toole, J. M., R. A. Krishfield, M.-L. Timmermans, and A. Proshutinsky (2011), The ice-tethered profiler: Argo of the Arctic, *Oceanography*, *24*(3), 126–135.
- Watanabe, E. (2011), Beaufort shelfbreak eddies and shelf-basin exchange of Pacific summer water in the western Arctic Ocean detected by satellite and modeling analyses, *J. Geophys. Res.*, *116*, C08034, doi:10.1029/2010JC006259.
- Watanabe, E., et al. (2014), Enhanced role of eddies in the Arctic marine biological pump, *Nat. Commun.*, *5*, 3950, doi:10.1038/ncomms4950.
- Woodgate, R. A., K. Aagaard, R. D. Muench, J. Gunn, G. Bjork, B. Rudels, A. T. Roach, and U. Schauer (2000), The Arctic Ocean boundary current along the Eurasian slope and the adjacent Lomonosov Ridge: Water mass properties, transports and transformations from moored instruments, *Deep Sea Res., Part I*, *48*, 1757–1792.